Averaged Stokes Vector Based Polarimetric SAR Data Interpretation

Fang Shang, *Member, IEEE,* and Akira Hirose, *Fellow, IEEE*

***Abstract*—In this paper, we propose a new polarimetric synthetic aperture radar data interpretation method based on locally averaged Stokes vector. We first propose a method to extract discriminators from all the three components of the averaged Stokes vector. Based on the extracted discriminators, we build four physical interpretation layers with ascending priorities: the basic structure layer, the low coherence targets layer, the man-made targets layer, and the low back scattering targets layer. An intuitive final image can be generated by simply stacking the four layers in priority order. We test the performance of the proposed method over ALOS-PALSAR data. The experimental results show that the proposed method has high interpretation performance, especially for skew aligned or randomly distributed buildings, and isolated man-made targets such as bridges.**

***Index Terms*—polarimetric SAR, Stokes vector, data interpretation.**

I. Introduction

Polarimetric synthetic aperture radar (PolSAR) system collects scattering information of observed targets. For classification applications, a high performance relies on reasonable and effective interpretation of PolSAR data. Interpretation methods with the potential to characterize generally existing partially polarized scattered wave [1]–[18] are widely used. Among them, decompositions based on coherency/covariance (C/T) matrix have aroused active discussions the most [1], [2], [4]–[7], [10], [11], [14]–[18].

Although the C/T matrix based decompositions are effective in many cases, there are still two main factors restricting their performances. Firstly, the C/T matrix cannot be used for extracting depolarization information of partially polarized scattered wave. Important depolarization information not only relates to the target features represented by the C/T matrix, but also relates to the polarization state of the incident wave [13]. To consider also such depolarization information from C/T matrix, in model-based decomposition methods, researchers introduced a volume scattering model. The expression of the model is switched according to the values of practical data to ensure high adaptability for various land situations. Nevertheless, depolarization phenomenon is caused in so many cases that finite number of volume models are not enough for all the situations. Thus, sometimes, the depolarization information cannot be reasonably estimated [19]. Secondly, in C/T matrix based decompositions, the averaged scattering mechanism described by the C/T matrix is decomposed as the sum of several elements. Such decomposition processes cannot be unique, complete, and physical, simultaneously. For example, the $H/A/\alpha$ decomposition [6], uniquely and completely decomposes the T matrix. However, since it is a mathematics based algorithm, the decomposition results are not convenient for the understanding with direct physical meanings [5]. On the contrary, the model-based decompositions decompose the T/C matrix into several elements corresponding to physical scattering models [5], [7], [10]. However, since the models are not totally independent, such physical decompositions are usually not unique or complete [5], [7], [11].

In this paper, we propose a new PolSAR data interpretation method based on locally averaged Stokes vector. The averaged Stokes vector describes the partially polarized scattered wave directly [13], [20]. In comparison with C/T matrix, it is a more powerful parameter for dealing with depolarization information. According to the well-known Born-Wolf wave decomposition [21], a partially polarized wave can be uniquely decomposed as the sum of a completely polarized wave and a completely unpolarized wave. Further, the decomposition is expressed by three physical components of the averaged Stokes vector: the total scattered intensity A, the degree of polarization (DoP) ρ, and the completely polarized wave component $\boldsymbol{G}^{PO}$. Note that decomposition here means the wave decomposition which obeys the general physical laws. It avoids the conflict among physical meaning, uniqueness, and completeness. The classification potentials of A and ρ have been proved in many works [13], [22]. In our previous works [23]–[25], we have introduced component $\boldsymbol{G}^{PO}$ into supervised classification process and obtained successful result. In this paper, we first propose the method to extract discriminators from all the three components. Based on the extracted discriminators, we propose four physical interpretation layers with ascending priorities: the basic structure layer, the low coherence targets layer, the man-made targets layer, and the low back scattering targets layer. On each layer, only targets with certain features are identified. Finally, an intuitive final image can be generated by simply stacking the four layers in priority order. We test the proposed method over ALOS-PALSAR data. The experimental results for Suruga bay area, Ebetsu city area, and Tokyo harbor area, show that the proposed method has high interpretation performance, especially for skew aligned or randomly distributed buildings, and isolated man-made targets such as bridges.

II. Averaged Stokes Vector

In this section, we first review the concept of the averaged Stokes vector for PolSAR data. After that, we analyze the averaged Stokes vector for classification application.

The authors are with the Department of Electrical Engineering and Information Systems, The University of Tokyo, Japan, Tokyo, 113-8656, e-mail: (shangfang@eis.t.u-tokyo.ac.jp; ahirose@ee.t.u-tokyo.ac.jp).

A. Concept of Averaged Stokes Vector

Fully PolSAR system measures 2×2 complex scattering matrix S for each resolution element:

$$S = \begin{bmatrix} S_{HH} & S_{HV} \\ S_{VH} & S_{VV} \end{bmatrix}, \tag{1}$$

where H and V represent horizontal and vertical polarization directions of antennas. In the case of backscattering in a reciprocal medium, $S_{HV} = S_{VH}$.

Scattering matrix relates the incident wave and scattered wave. It is a parameter for observed target. Contrarily, the averaged Stokes vector describes the polarization state of electromagnetic radiation. It is a parameter for wave. Therefore, to calculate the averaged Stokes vector for scattered wave from PolSAR data, a certain incident wave needs to be supposed. This incident wave is expressed by a unit Jones vector $[E_H^i \;\; E_V^i]^T$ which is given by

$$\begin{bmatrix} E_H^i \\ E_V^i \end{bmatrix} = \begin{bmatrix} \cos\phi & -\sin\phi \\ \sin\phi & \cos\phi \end{bmatrix} \begin{bmatrix} \cos\tau \\ j\sin\tau \end{bmatrix}, \tag{2}$$

where $\phi \in \left[-\frac{\pi}{2}, \frac{\pi}{2}\right]$ and $\tau \in \left[-\frac{\pi}{4}, \frac{\pi}{4}\right]$ are orientation angle and aperture angle describing polarization state of the incident wave.

The scattered wave $[E_H^r \;\; E_V^r]^T$ is obtained by

$$\begin{bmatrix} E_H^r \\ E_V^r \end{bmatrix} = \begin{bmatrix} S_{HH} & S_{HV} \\ S_{VH} & S_{VV} \end{bmatrix} \begin{bmatrix} E_H^i \\ E_V^i \end{bmatrix}. \tag{3}$$

The Jones coherency matrix J is defined as

$$J = \begin{bmatrix} \langle E_H^r E_H^{r*} \rangle & \langle E_H^r E_V^{r*} \rangle \\ \langle E_V^r E_H^{r*} \rangle & \langle E_V^r E_V^{r*} \rangle \end{bmatrix} = \begin{bmatrix} J_{HH} & J_{HV} \\ J_{VH} & J_{VV} \end{bmatrix}, \tag{4}$$

where $\langle \cdot \rangle$ indicates spatial averaging process in a local window. From the Jones coherency matrix, the averaged Stokes vector $\boldsymbol{G}$ is defined as

$$\boldsymbol{G} = \begin{bmatrix} g_0 \\ g_1 \\ g_2 \\ g_3 \end{bmatrix} = \begin{bmatrix} J_{HH} + J_{VV} \\ J_{HH} - J_{VV} \\ J_{HV} + J_{VH} \\ j(J_{HV} - J_{VH}) \end{bmatrix}. \tag{5}$$

Generally, this averaged Stokes vector expresses a partially polarized wave. According to the Born-Wolf wave decomposition [21], the averaged Stokes vector can be regarded as the sum of a completely polarized wave and a completely unpolarized wave. Physically, the relationship between these two parts of information is expressed as [3], [13], [20]

$$\begin{aligned} \boldsymbol{G} &= A\left[\rho \boldsymbol{G}^{PO} + (1-\rho)\,\boldsymbol{G}^{UN}\right] \\ &= A\left\{\rho \begin{bmatrix} 1 \\ \tilde{g}_1 \\ \tilde{g}_2 \\ \tilde{g}_3 \end{bmatrix} + (1-\rho) \begin{bmatrix} 1 \\ 0 \\ 0 \\ 0 \end{bmatrix}\right\}, \end{aligned} \tag{6}$$

where $\tilde{g}_1^2 + \tilde{g}_2^2 + \tilde{g}_3^2 = 1$. $\boldsymbol{G}^{PO}$ and $\boldsymbol{G}^{UN}$ represent Stokes vectors for completely polarized wave and completely unpolarized wave, respectively, A is total scattered intensity, and ρ is degree of polarization which can be calculated as

$$\rho = \frac{\sqrt{g_1^2 + g_2^2 + g_3^2}}{g_0}. \tag{7}$$

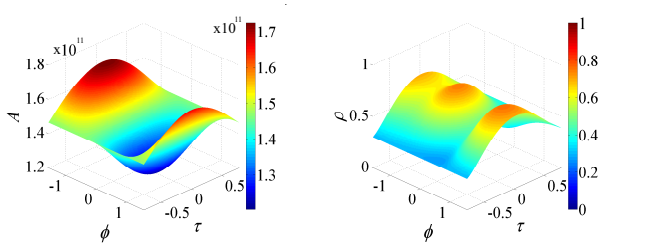

(a) (b)

Fig. 1. (a) Total scattered intensity and (b) DoP for the sample window data with all the orientation angle ϕ and aperture angle τ.

Since J is a complex Hermitian positive semidefinite matrix, it follows $g_1^2 + g_2^2 + g_3^2 \leq g_0^2$. So that, $0 \leq \rho \leq 1$.

According to (6), the averaged Stokes vector carries both of the completely polarized, and completely unpolarized wave information. The averaged Stokes vector is a powerful parameter to describe a partially polarized scattered wave in PolSAR observation.

B. Analysis of Averaged Stokes Vector

The averaged Stokes vector has three independent components: total scattered intensity A, degree of polarization ρ, and completely polarized wave part $\boldsymbol{G}^{PO}$. They are variables related to the polarization state of the incident wave. Mathematically, according to (2), these three components are variables of orientation angle ϕ and aperture angle τ. To illustrate the features of A, ρ, and $\boldsymbol{G}^{PO}$, we show these three components for a sample window of ALOS-PALSAR data. Note that, window size for spatial averaging process in (4) directly affects the calculation result of the corresponding Stokes vector. In our previous work [23], we showed that the size of a square window should be at least 5×5 to obtain Stokes vector with reliable DoP information for ALOS-PALSAR data. Considering the fact that larger window size will lead to lower resolution after averaging process, we finally chose 5×5 window in [23]. In this paper, keeping the total pixel number around 25, we have further optimized the side lengths (in pixels) of the window. We have tested the window sizes (range direction $\times$ azimuth direction) 2×12, 3×8, 4×6, and 5×5. We have found that the best window size is 3 (range) $\times$ 8 (azimuth direction) in pixels. The values of scattering matrices in the sample window are shown in Table I. According to (1) to (6), we can calculate A, ρ, and $\boldsymbol{G}^{PO}$ for this window.

Fig. 1 shows the values of total scattered intensity A and degree of polarization ρ with various ϕ and τ calculated for the sample window data. There, A and ρ are scalars varying with the changes of ϕ and τ. Normally, instead of considering all of these values, only several special values are used in classification processes. For example, in [13], the authors construct discriminators for the classification process by using the maximum and minimum values of A.

Completely polarized wave component $\boldsymbol{G}^{PO}$ is a 3 dimensional vector. The $\boldsymbol{G}^{PO}$ for a certain polarization state of incident wave, i.e. , certain values of ϕ and τ, can be

TABLE I
ALOS-PALSAR DATA IN A 3×8 SAMPLE WINDOW

S_{HH} *data* $(\times 10^5)$							
0.11+0.55j	-0.31-1.77j	1.28-0.03j	1.92+0.35j	-0.53-1.20j	1.28-0.35j	1.62+0.89j	-2.36+1.73j
2.14-1.70j	-0.37+1.08j	1.71+0.83j	2.23-0.10j	-0.54+2.49j	-2.33+1.43j	-2.72-2.41j	-2.41-4.23j
-1.92-0.92j	1.19-1.50j	1.97+0.40j	0.14-0.39j	-0.48-0.02j	7.25-4.56j	4.34-5.18j	1.34+4.23j
$S_{HV} = S_{VH}$ *data* $(\times 10^5)$							
-0.76-0.88j	-1.32-0.10j	-1.19+0.31j	-1.05-0.08j	0.76-0.85j	1.37-1.53j	-0.92-1.11j	-1.24-0.19j
0.27+0.25j	1.92+0.01j	0.87+0.06j	-0.91+0.33j	-0.68-1.84j	0.29-1.10j	0.57-0.22j	-1.74+0.00j
0.16-0.39j	-0.91-0.59j	-0.66+0.55j	-0.49+1.58j	0.43+2.92j	-0.75+1.23j	-2.23+2.79j	-0.14+1.59j
S_{VV} *data* $(\times 10^5)$							
0.57+3.64j	1.56-0.38j	0.20-2.48j	-1.47-0.62j	-1.19-1.66j	1.00-1.47j	2.59-0.76j	0.19-1.18j
1.15+0.75j	-0.19+1.10j	0.70+2.49j	-1.43+1.13j	-1.84+2.73j	1.24+1.31j	-0.91-1.22j	-1.28-3.14j
-3.26+3.23j	-2.78+0.93j	-1.36-0.67j	-1.76+0.09j	-4.29+0.53j	4.86-1.97j	6.27-0.31j	3.35+11.18j

expressed by a point on the Poincare sphere. With the change of ϕ and τ, a set of such points form particular routes on the Poincare sphere. We can observe these routes in two ways: for series of constant ϕ with continuously varying τ, and for series of constant τ with continuously varying ϕ. They are named orientation routes and aperture routes, respectively. The orientation routes and aperture routes for the sample window are shown in Fig. 2a and b, respectively. The routes cover the whole Poincare sphere. Similar to the situation of A and ρ, it is difficult and actually no need for us to consider all the routes in a classification process. We can only select special ones among them. Thus, we select two special routes. As shown in Fig. 2c, they are the orientation route for $\phi = 0$ (red) and the aperture route for $\tau = 0$ (green). They are named zero orientation route and zero aperture route, respectively. These two routes carry plentiful polarization information.

The averaged Stokes vector in (6) represents a concept for partially polarized wave caused by incoherent target. Therefore, such an averaged Stokes vector cannot be related to a certain scattering matrix which represents a concept for coherent target. However, in ideal situation, completely polarized wave component should be related to a certain scattering matrix. That is to say, an actual route should be approximated to an ideal route which can be perfectly related to a certain scattering matrix.

In Appendix A, we prove that the ideal routes are always circular arcs on the Poincare sphere. Mathematically, circular arcs can be determined by 3 non-collinear points. We can use the ideal route determined by any three points on an actual route as the approximated route. However, to guarantee reliability and preserve most polarization information, we use $\boldsymbol{G}^{PO}$ for horizontal $(\phi = 0, \tau = 0)$, left circular $(\phi \in [-\pi/2, \pi/2], \tau = \pi/4)$, and right circular $(\phi \in [-\pi/2, \pi/2], \tau = -\pi/4)$ polarized incident wave, noted as $\boldsymbol{G}_H^{PO}$, $\boldsymbol{G}_{lc}^{PO}$, and $\boldsymbol{G}_{rc}^{PO}$, to determine an ideal zero orientation route. Similarly, the use of $\boldsymbol{G}^{PO}$ for horizontal, 45° $(\phi = \pi/4, \tau = 0)$, and -45° $(\phi = -\pi/4, \tau = 0)$ polarized incident wave, noted as $\boldsymbol{G}_H^{PO}$, $\boldsymbol{G}_{45^\circ}^{PO}$, and $\boldsymbol{G}_{-45^\circ}^{PO}$, uniquely determines an ideal zero aperture route. Here, $\boldsymbol{G}_H^{PO}$ is always the cross point of the zero orientation and zero aperture routes, while $\boldsymbol{G}_{lc}^{PO}$ and $\boldsymbol{G}_{rc}^{PO}$ are two terminal points of the zero orientation route. The ideal routes determined by these five points are shown by the pink and blue curves in Fig. 2c. Thus, we can use the ideal routes to express the features of the actual routes. In detail, we can analyze the geometrical features of the orientation triangle and aperture triangle determined by the give points, as shown in Fig. 2d, to get the information of $\boldsymbol{G}^{PO}$ for the sample window.

III. AVERAGED STOKES VECTOR BASED DISCRIMINATORS

We use ALOS-PALSAR 1.1 level data for Suruga bay area in the following experiments. The color composite polarimetric image of the test area is shown in Fig. 3a. The test area mainly includes a sea area (right), an urban area (middle), a forest area (left), and in the urban area, there is a large farmland area. The window size for calculating averaged Stokes vector is 3×8 in pixel. The window moving steps are 1 pixel in both of the range and azimuth directions. From the three components of the averaged Stokes vector, A, ρ, and $\boldsymbol{G}^{PO}$, we can construct various discriminators. In some works, such as [13], [22], authors focus on only the scalar components A and ρ. In our previous work [19], we suggested several discriminators constructed by the vector component $\boldsymbol{G}^{PO}$. Besides these proposed ones, we keep on constructing and testing many more discriminators. Finally, we selected five important discriminators. They are: averaged intensity A_m, averaged degree of polarization ρ_m, perimeter degree of zero orientation route PD_{or}, inclination degree of zero aperture route ID_{ap}, and arc asymmetry degree of zero aperture route AAD_{ap}.

A. Averaged Intensity

To make the total intensity component A convenient for use, first we define the normalized intensity for ALOS-PALSAR data as

$$A^{norm} = 1 - e^{-10^{-11}A}, \tag{8}$$

where $A^{norm} \in (0, 1)$, the coefficient 10^{-11} is chosen because the order of magnitude of A (which is proportional to $|S|^2$) for ALOS-PALSAR Data is 10^{11}. The averaged intensity is

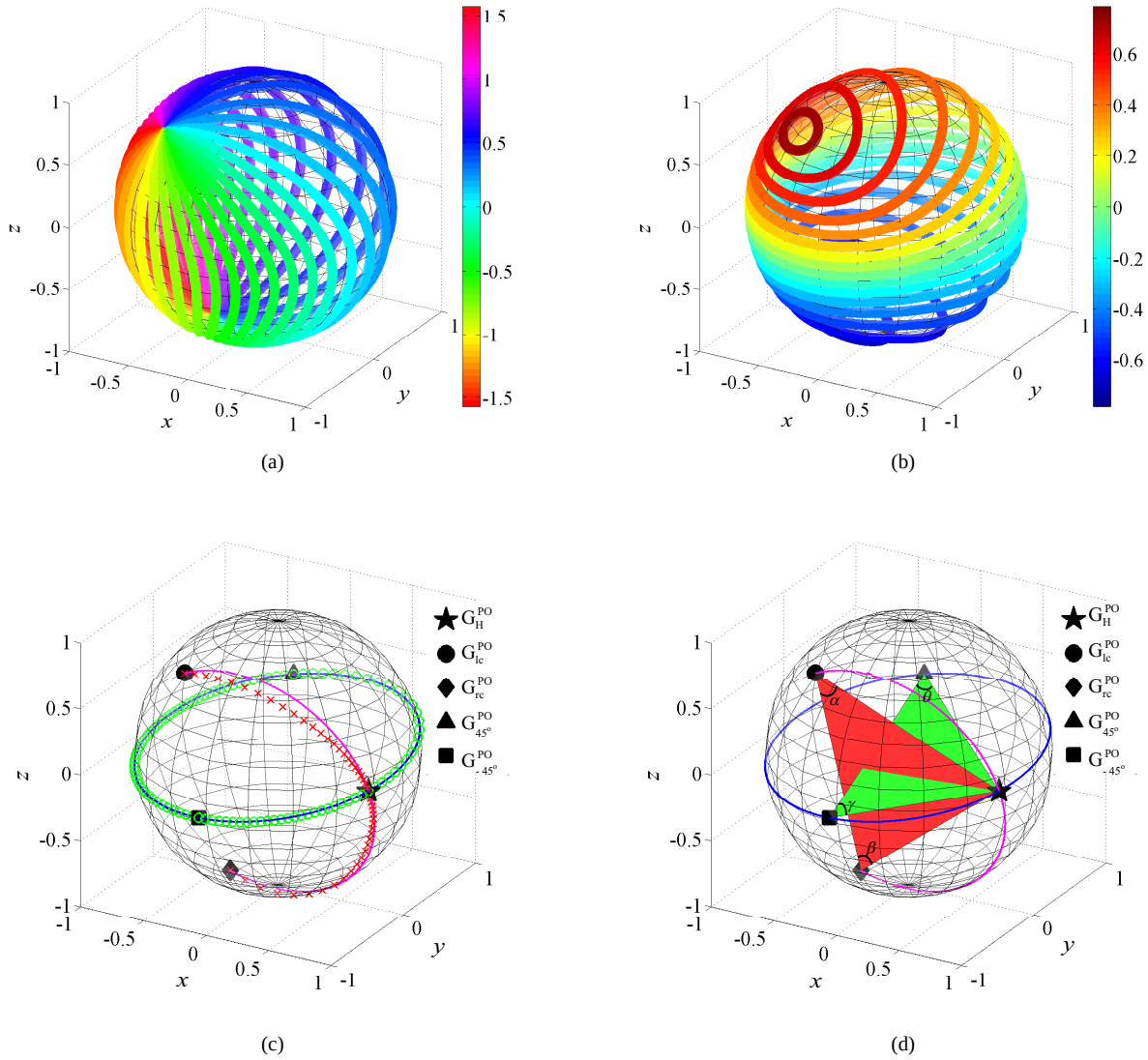

Fig. 2. (a) Orientation routes; (b) aperture routes; (c) actual zero orientation route (red crosses) and zero aperture route (green circles) and the ideal zero orientation route (pink curve) and zero aperture route (blue curve) determined by the five points: $\boldsymbol{G}_H^{PO}$, $\boldsymbol{G}_{lc}^{PO}$, $\boldsymbol{G}_{rc}^{PO}$, $\boldsymbol{G}_{45°}^{PO}$, $\boldsymbol{G}_{-45°}^{PO}$; and (d) orientation triangle (red) and aperture triangle (green), all for the sample window.

defined as

$$A_m = \frac{1}{5}\left(A_H^{norm} + A_{lc}^{norm} + A_{rc}^{norm} + A_{45°}^{norm} + A_{-45°}^{norm}\right), \tag{9}$$

where A_H^{norm}, A_{lc}^{norm}, A_{rc}^{norm}, $A_{45°}^{norm}$, $A_{-45°}^{norm}$ are the normalized intensity for horizontal, left circular, right circular, $45°$, and $-45°$ polarized incident wave. The averaged intensity for Suruga bay area is shown in Fig. 3b. The discriminator A_m is very sensitive to the topography of the test area. Especially, as shown in Fig. 3b, the A_m shows low value in backlighting areas (one side of the mountains) and plane areas (the farmland and the sea areas).

B. Averaged Degree of Polarization

The averaged degree of polarization is defined as

$$\rho_m = \frac{1}{5}\left(\rho_H + \rho_{lc} + \rho_{rc} + \rho_{45°} + \rho_{-45°}\right), \tag{10}$$

where ρ_H, ρ_{lc}, ρ_{rc}, $\rho_{45°}$, and $\rho_{-45°}$ are the degree of polarization for horizontal, left circular, right circular, $45°$, and $-45°$ polarized incident wave. The averaged degree of polarization for Suruga bay area is shown in Fig. 3c. The discriminator ρ_m reflects coherence of the targets in an observing window. As shown in Fig. 3c, ρ_m has high values for coherent targets, such as the sea area, whereas low value for incoherent targets, such as the forest area.

C. Perimeter Degree of Zero Orientation Route

According to Fig. 2d, the perimeter degree of zero orientation route PD_{or} is defined by

$$PD_{or} = \frac{\alpha + \beta}{\pi}. \tag{11}$$

The PD_{or} is calculated from the approximated ideal zero orientation route. This ideal route can be related to a scattering

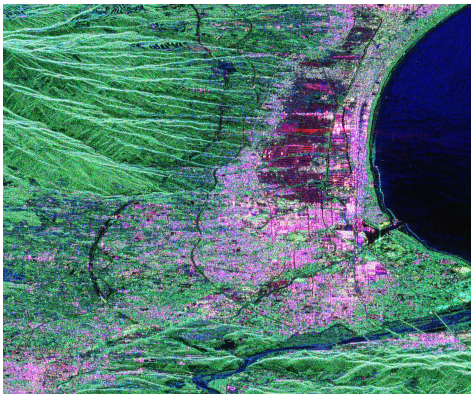

(a) Color composite polarimetric image

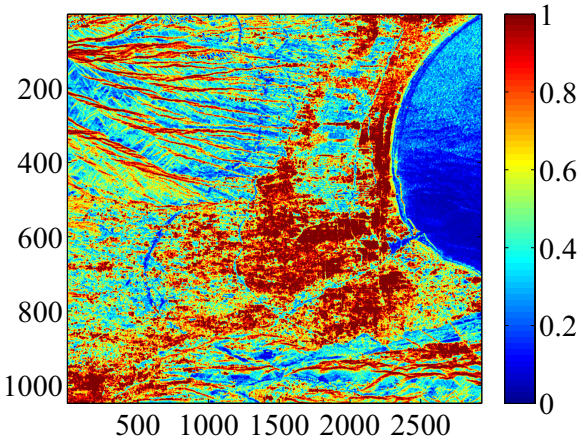

(b) Averaged intensity A_m

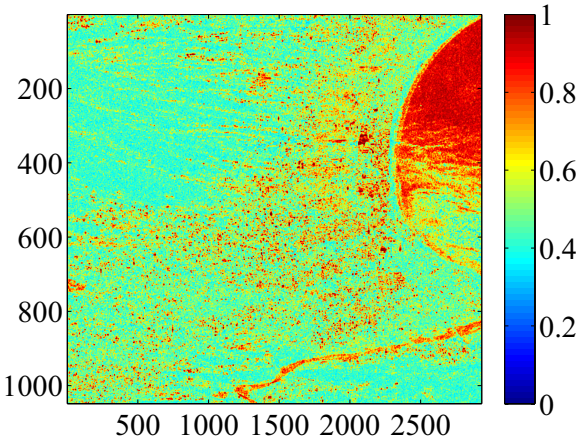

(c) Averaged degree of polarization ρ_m

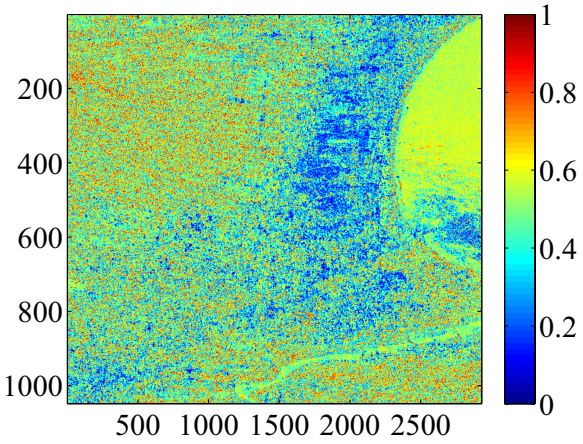

(d) Perimeter degree of zero orientation route PD_{or}

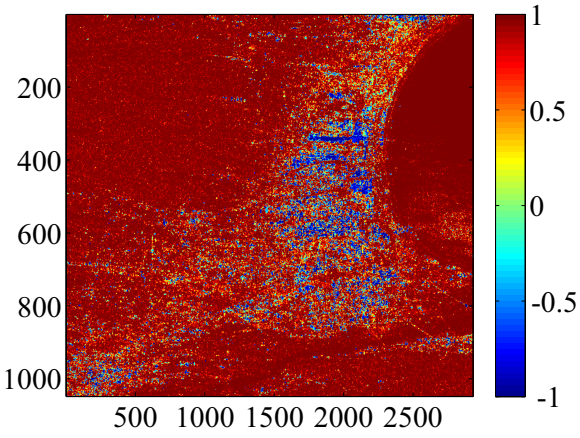

(e) Inclination degree of zero aperture route ID_{ap}

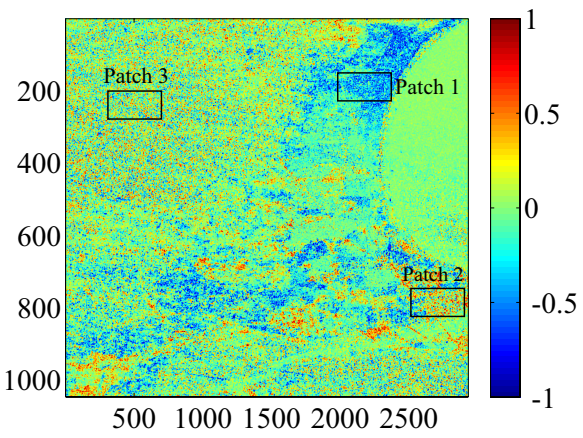

(f) Arc asymmetry degree of zero aperture route AAD_{ap}

Fig. 3. (a) The color composite polarimetric image for Suruga bay area: R=$\frac{1}{2}|S_{HH} - S_{VV}|^2$, G=$2|S_{HV}|^2$, B=$\frac{1}{2}|S_{HH} + S_{VV}|^2$, and (b)-(f) averaged Stoke vector based discriminators.

matrix S_0 given by

$$S_0 = \begin{bmatrix} a & b \\ c & d \end{bmatrix}, \tag{12}$$

which represents the main scattering mechanism in a local observed window. We can understand the physical meaning of PD_{or} by considering the relationship between PD_{or} and S_0. We can first consider the reflection symmetry condition: $b \approx c$ and $ab^* \approx db^* \approx 0$ [5] to find out the dominant relationship

which is given by

$$PD_{or} \approx 1 - \frac{1}{\pi}\arccos\left(\frac{dd^* - aa^*}{dd^* + aa^*}\right), \tag{13}$$

where aa^* and dd^* represent the scattered power in HH and VV channels for S_0. If the medium is horizontal dipole dominant ($aa^* \gg dd^*$), PD_{or} will be near to 0. If it is vertical dipole dominant ($aa^* \ll dd^*$), PD_{or} will be near to 1. If horizontal dipole and vertical dipole are almost balanced ($aa^* \approx dd^*$), PD_{or} will be around 0.5. Thus, the value of PD_{or} indicates basic structure features of observed targets. For the general situation (no limitation of $|b|$ and $|c|$), the relationship in (13) becomes very complicated. However, the physical meaning of PD_{or} is similar.

The PD_{or} for Suruga bay area is shown in Fig. 3d. In the figure, high values of PD_{or} appear in forest area, whereas low values of PD_{or} appear in farmland area. Possibly, the reason for this phenomenon is that L band wave of ALOS-PALSAR penetrates most of the branches, leaves, and crops. For forest and farmland areas, the ALOS-PALSAR data mainly shows the information of trunks (vertical dipole dominant) and furrows (horizontal dipole dominant). We need to note that, horizontal and vertical here are defined by antenna coordinate system, not the local coordinate system for the target. Between these two coordinate systems, there is usually a small rotation angle difference.

D. Inclination Degree of Zero Aperture Route

The inclination degree of zero aperture route is defined as

$$ID_{ap} = \frac{\boldsymbol{G}^{PO}_{45^\circ}(y) - \boldsymbol{G}^{PO}_{-45^\circ}(y)}{|\boldsymbol{G}^{PO}_{45^\circ} - \boldsymbol{G}^{PO}_{-45^\circ}|}, \tag{14}$$

where $\boldsymbol{G}^{PO}_{45^\circ}(y)$ and $\boldsymbol{G}^{PO}_{-45^\circ}(y)$ are the projections on y-axis of $\boldsymbol{G}^{PO}_{45^\circ}$ and $\boldsymbol{G}^{PO}_{-45^\circ}$. The discriminator ID_{ap} describes attitude of zero aperture route in the Poincare sphere space. Again, considering the reflection symmetry condition: $b \approx c$ and $ab^* \approx db^* \approx 0$, we can find that the main relationship between ID_{ap} and components of S_0 is given by

$$ID_{ap} \approx \frac{Re(ad^*)}{|a||d|}, \tag{15}$$

where $Re(ad^*)$ indicates the real part of the complex number ad^*. In [5], sign of $Re(ad^*)$ is used to decide whether strong double bounce scattering exists. Similarly, ID_{ap} is also a discriminator closely related to such a scattering mechanism. Negative value of ID_{ap} appears in strong double bounce scattering dominant areas. The inclination degree of zero aperture route ID_{ap} for Suruga bay area is shown in Fig. 3e. In this figure, ID_{ap} shows negative value in farmland and part of the urban areas.

E. Arc Asymmetry Degree of Zero Aperture Route

The arc asymmetry degree of zero aperture route is defined as

$$AAD_{ap} = \frac{\gamma - \theta}{\gamma + \theta}, \tag{16}$$

where γ and θ are shown in Fig. 2d. They are the interior angles of the aperture triangle. The arc asymmetry degree of zero aperture route AAD_{ap} for Suruga bay area is shown in Fig. 3(f). The discriminator AAD_{ap} describes the asymmetry feature of the targets in an observing window. If the targets are almost symmetry with radar illumination, the value of AAD_{ap} will be near to 0. Otherwise, the value will deviate much from 0. As shown in Fig. 3f, very high value or very low value of AAD_{ap} appears in highly randomly distributed targets area, such as the forest area and parts of the urban area.

IV. PolSAR Data Interpretation

The above A_m, ρ_m, PD_{or}, ID_{ap}, and AAD_{ap} are five important Stokes vector based discriminators. These five discriminators are already the interpretation results which can be used in the further classification process, similar to that in other works [26]–[29]. To show the interpretation results intuitively, normally, we also need to generate a final interpretation image. However, the conventional RGB presentation as shown in [5], [7] is not suitable in our case. The first reason is that we have five discriminators, more than three. The RGB representation is not enough. The second reason is that, in Y4R, all the discriminators are intensities. It is reasonable to combine them in one image by RGB representation. Whereas our discriminators have totally different physical meanings. It is unreasonable to combine all of them in one image simultaneously. Therefore, in this paper, we proposed physical interpretation layers for generating final image.

A. Physical Interpretation Layers

In the proposed method, we further analyze the discriminators to build four layers serving as interpretation results of a target area. In each layer, we focus only on targets with one certain physical feature. The information provided in each layer has unequal priority. These four layers are elaborated as follows:

1) Basic Structure Layer (Layer 1): In this layer, we use the discriminator PD_{or} to show the basic structure information. Such basic structure information is the most general information which can be provided by all the targets. So that, this layer has the lowest priority in all the layers. The basic structure layer for Suruga bay area is shown in Fig. 4a. Basically, Fig. 4a is the same as Fig. 3d. However, to avoid color conflict with other layers, we use different RGB code for Fig. 4a which is defined as

$$(R,G,B) = \begin{cases} (1-2PD_{or}, 1-2PD_{or}, 2PD_{or}) & \text{if } PD_{or} \le 0.5 \\ (0, 2PD_{or}-1, 1) & \text{if } PD_{or} > 0.5 \end{cases}, \tag{17}$$

where $R,G,B \in [0,1]$. According to the color code in (17) and the physical meaning of PD_{or} described in Section III-C, we know that horizontal structure dominant medium will show yellow color, vertical structure dominant medium will show aqua color, and surface/plane medium will show blue color on this layer.

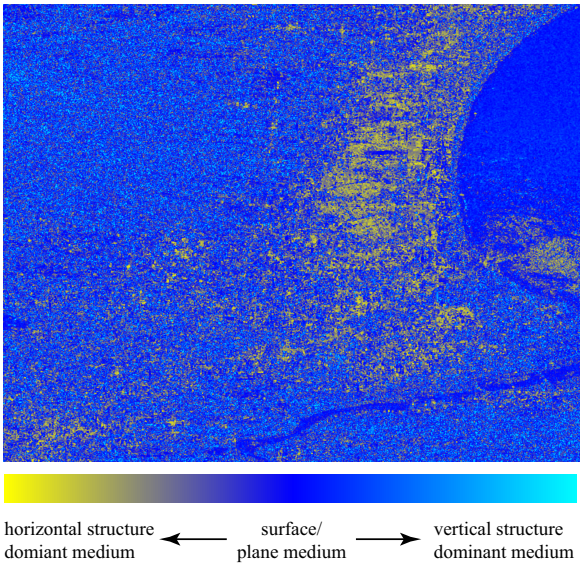

(a) Layer 1: Basic structure layer

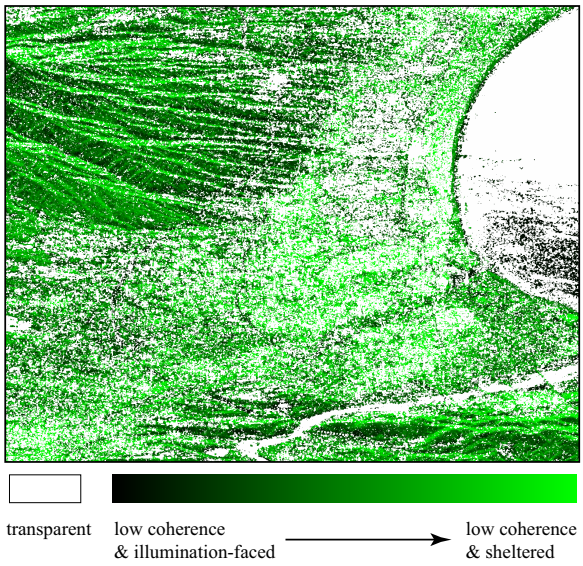

(b) Layer 2: Low coherence targets layer

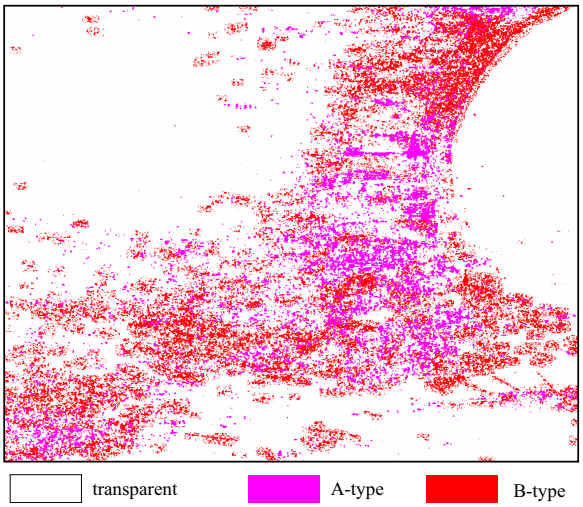

(c) Layer 3: Man-made targets layer

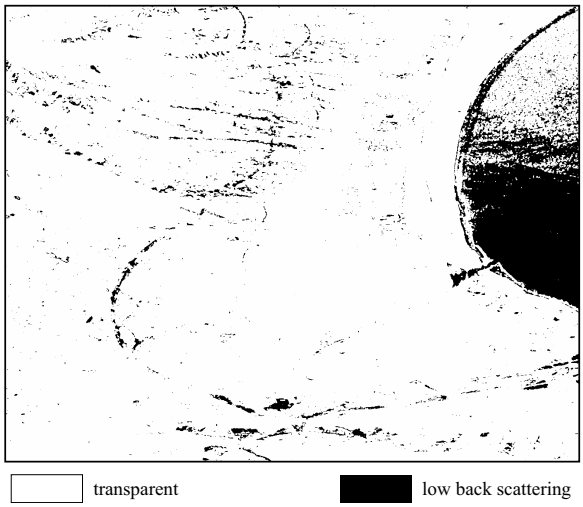

(d) Layer 4: Low back scattering targets layer

Fig. 4. Interpretation layers generated by ALOS-PALSAR data with thresholds: $\delta_\rho = 0.5$, $\delta_h = 0.3$, $\delta_w = 0.4$, $\delta_A = 0.2$, and patch size of W: 15×60, for Suruga bay area.

2) Low Coherence Targets Layer (Layer 2): In Layer 1, we only consider the discriminator PD_{or} which is constructed by the completely polarized wave component $\boldsymbol{G}^{PO}$ of Stokes vector. However, according to (6), for highly incoherent targets (ρ is low), the weight of completely unpolarized wave component $\boldsymbol{G}^{UN}$ will be high. So that, the effect of $\boldsymbol{G}^{UN}$ will be more significant than $\boldsymbol{G}^{PO}$.

In low coherence targets layer, we identify low coherence targets by using the value of discriminator ρ_m as the criterion. We additionally use the discriminator A_m to show topography information for these identified low coherence targets. According to the topography information, we can understand whether the low coherence targets are illumination-faced or sheltered. Here, illumination-faced, and sheltered faced targets mean the targets with topographies corresponding to small, and large local incident angels, respectively. This layer has higher priority than Layer 1 since it shows more specific information. The color code is defined as

$$(R, G, B) = \begin{cases} (0, A_m, 0) & \text{if } \rho_m \leq \delta_\rho \\ transparent & \text{if } \rho_m > \delta_\rho \end{cases}. \qquad (18)$$

For ALOS-PALSAR data, $\delta_\rho = 0.5$ is used as the threshold. The low coherence targets layer for Suruga bay area is shown in Fig. 4b. In Fig. 4b, all the low coherence targets are colored as green with different brightnesses, while the high coherence targets ($\rho_m > \delta_\rho$) remain transparent. The brightness of green color indicates the topography information of the low coherence target. The sheltered low coherence targets show dark green color, and illumination-faced low coherence targets have light green color.

3) Man-Made Targets Layer (Layer 3): In this layer, we identify man-made targets. In comparison with Layer 1 and Layer 2, the information provided in Layer 3 is highly specific.

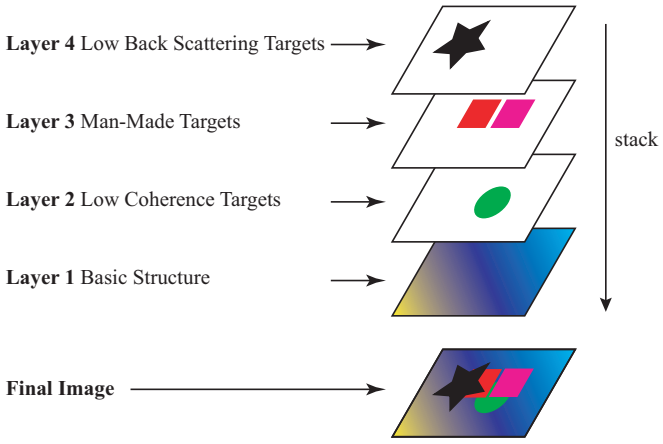

Fig. 5. Sketch of final image generating process

Therefore, Layer 3 has higher priority than them.

The first category of man-made targets are those orthogonal to radar illumination (A-type man-made targets). Such man-made targets lead to strong double bounce scattering. We can easily detect the targets with strong double bounce scattering according to the physical meaning of ID_{ap} described in Section III-D. Nevertheless, some natural targets also lead to strong double bounce scattering, such as farmland area orthogonal to radar illumination. To distinguish those two types of targets, we need to consider the scattered intensity. Normally, A-type man-made targets cause much stronger scattered intensity than natural targets. Thus, we can use discriminator ID_{ap} and A_m together to identify A-type man-made targets. The RGB code is defined as

$$(R,G,B) = \begin{cases} (1,0,1) & \text{if } ID_{ap} \leq 0 \text{ and } A_m > 0.5 \\ transparent & \text{otherwise} \end{cases}. \tag{19}$$

The second category of man-made targets are skew aligned or randomly distributed ones (B-type man-made targets). B-type man-made targets cannot be identified by using (19), since observable double bounce scattering is very weak in such areas. An important feature of B-type man-made target is that it is asymmetrical to radar illumination. Thus, the discriminator AAD_{ap} will show high absolute value for such target. However, according to Fig. 3f, high absolute values appear not only in man-made targets areas (Patch 1 and Patch 2), but also in natural low coherence area such as forest area (Patch 3). Comparing Patch 1/2 and Patch 3, we can find that high absolute values in Patch 1 and Patch 2 are obviously biased, i.e., evenly positive, or evenly negative. However, Patch 3 shows the mixture of positive and negative values. To distinguish between B-type man-made targets and natural low coherence targets, we define a bias detection function f_{bias} for a small local patch W as

$$f_{bias}(W) = \frac{|\sum_{i=1}^{N} AAD_{ap}(h_i)|}{N}, \tag{20}$$

where $f_{bias} \in (0,1)$, the set $\{h_i\}$ is defined as $\{h_i \in W : |AAD_{ap}(h_i)| > \delta_h\}$, $AAD_{ap}(h_i)$ is the value of discriminator AAD_{ap} for point h_i, N is the total number of elements in the set $\{h_i\}$, and $\delta_h \in (0,1)$ is a threshold for selecting pixels with AAD_{ap} values deviating much from 0, which represent possible man-made targets according to the analysis in Section III-E.

Thus, for a pixel w in the small local patch W, we can define the RGB value as

$$(R,G,B) = \begin{cases} (1,0,0) & \text{if } f_{bias}(W) > \delta_w \text{ and } w \in \{h_i\} \\ transparent & \text{otherwise} \end{cases}, \tag{21}$$

where $\delta_w \in (0,1)$ is the threshold for determining whether the small local patch can be determined as man-made targets area.

Note that, in (17) to (19), the operation unit is one pixel on discriminator image as shown in Fig. 3. Differently, the operation unit in (21) is a small local patch, i.e., for detecting B-type man-made targets, we consider not only the value of AAD_{ap}, but also its local distribution. The size of local patch W need to be selected carefully. Too large size will lead to low resolution, while too small size is not enough to show the numerical distribution. In experiments, we found that 15×60 (range direction $\times$ azimuth direction) is the best for ALOS-PALSAR data. It corresponds to roughly a 200m$\times$ 200m area on ground which is a scale enough to include several buildings. The threshold δ_h is used for detecting all the possible man-made target pixels. If the threshold is too high, we cannot detect all the possible pixels, while if it is too low, we will include many pixels which have too low possibilities to be man-made targets. After testing many samples from B-type man-made targets, we found that $\delta_h = 0.3$ is the best. The threshold δ_w is used for judging that whether the numerical distribution of all the detected possible pixels in W is biased enough to determine W as a B-type man-made targets area. Also by testing for many samples, we found that $\delta_w = 0.4$ is the best. These parameters are available to all the ALOS-PALSAR data. Finally, the man-made targets layer for Suruga bay area is shown in Fig. 4c.

4) Low Back Scattering Targets Layer (Layer 4): If the back scattering intensity is very low, the received signal is affected by various noise. Thus, for such areas, the identified result in Layer 1, Layer 2 and Layer 3 are not reliable. Therefore, in the layer with highest priority, we need to identify targets with low reflection by considering discriminator A_m. The RGB code for layer 4 is defined as

$$(R,G,B) = \begin{cases} (0,0,0) & \text{if } A_m \leq \delta_A \\ transparent & \text{if } A_m > \delta_A \end{cases}. \tag{22}$$

For ALOS-PALSAR data, $\delta_A = 0.2$ is used as the threshold. The low reflection targets layer for Suruga bay area is shown in Fig. 4d.

Note that the expressions (17) to (22) are available for all the fully PolSAR data. However, thresholds δ_ρ, δ_h, δ_w, δ_A, and patch size of W need to be calibrated for different PolSAR system. In Table II we summarize all these thresholds and patch size for ALOS-PALSAR data.

The parameters in Table II are available for general cases of ALOS-PALSAR application. The thresholds δ_ρ and δ_A can be also slightly adjusted for certain application purposes. For example, if we need to pay significantly more attention to

TABLE II
THRESHOLDS AND PATCH SIZE FOR ALOS-PALSAR DATA

$\delta_{rho} = 0.5$	$\delta_h = 0.3$
$\delta_w = 0.4$	$\delta_A = 0.2$
patch size of W: 15×60	

structure information than low coherence information in some applications, we can make the threshold δ_ρ lower than 0.5.

B. Intuitive Final Interpretation Image

We can generate an intuitive final image by stacking the four layers according to priority order. A layer with higher priority is stacked on a layer with lower priority. The sketch of the stacking process is shown in Fig. 5. According to the sketch, we can find that, if a pixel is identified (colored) on several layers, the color in an upper layer will cover the color in a lower layer. It means that, only the information with highest priority is shown in final image. In this way, we obtain final interpretation image for Suruga bay area as shown in Fig. 6a.

We can understand Fig. 6a in the following way. If the color for basic structure layer is shown in a pixel, it means that the targets in this pixel does not have obvious features considered in the upper layers (low coherence, man-made and low back scattering). Thus, targets are interpreted as natural high coherence targets such as farmland and the sea. Similarly, if the color for low coherence targets layer is shown, it indicates the targets are natural low coherence targets such as forest. If the color for man-made targets layer is shown, it clearly represents the man-made targets. If the color for low back scattering targets layer is shown, it corresponds the existence of smooth surface targets such as peaceful sea.

V. DISCUSSION

To show the classification potential of the proposed method, we choose the four-component scattering power decomposition with rotation of coherency matrix described in [10] (noted as Y4R in the following text) for comparison. An important common point of these two methods is that both of them are physical interpretations for PolSAR data. The Y4R method provides four discriminators which present scattering intensities of surface, double bounce, volume, and helix models. Our proposed method provides five discriminators shown in (9), (10), (11), (14), (16). These five discriminators describe different physical meanings of the targets. For generating intuitive final interpretation image, in Y4R method, RGB representation is employed, where the scattering intensities of double bounce, volume, and surface models are used to correspond R, G, and B values, respectively. In our method, we proposed physical layers for generating final interpretation image. Though basic ideas of our proposed method and that of Y4R are different, they are still comparable.

The decomposition result of Y4R method for Surugabay area is shown in Fig. 6b. This image is generated with the same process and parameter set described in [10]. Comparing Figs. 6a and 6b, we find that both of the methods have high interpretation performance. Especially, the proposed method shows higher performance on detecting man-made targets as follows.

We can zoom in Patch A, a city area, shown in Fig. 6a. The Google satellite photo and the interpretation results obtained by the proposed method and Y4R method for Patch A are shown in Fig. 7a, b, and c, respectively. Color codes for Fig. 7 are the same as those shown in Fig. 6. In Fig. 7b, the city area can be correctly and clearly identified, whereas, in Fig. 7c, most pixels in the city area are interpreted as volume scattering dominant area (green). This interpretation is basically reasonable, since such skew aligned or randomly distributed city area is a highly incoherent target which leads to high volume scattering power. However, such scattering mechanism (volume dominant) is evidently different from the typical scattering mechanism for a city area (double bounce), but really close to that for a forest area (volume dominant). Thus, in further classification process, it is very difficult to distinguish between such skew aligned or randomly distributed man-made targets and forest targets.

Moreover, we can zoom in Patch B, an area include bridges, shown in Fig. 6a. The Google satellite photo and the interpretation results obtained by the proposed method and Y4R method for Patch B are shown in Fig. 7d, e, and f, respectively. In Fig. 7e, the bridges can be correctly identified as man-made targets, whereas, in Fig. 7f, the bridges show a volume dominant scattering mechanism. Since the main scattering mechanism for bridges should be double bounce dominant, such a volume dominant result is not reasonable.

Fig. 7 indicates the high performance of the proposed method for skew aligned or randomly distributed man-made targets and isolated man-made targets in Suruga bay area. We have done the comparison for many areas to verify the performance of the proposed method. We take results for Ebetsu city area and Tokyo harbor area as examples. The Ebetsu city area, shown in Fig. 8a, includes a forest park and a city area adjacent to each other. In comparison with the result of Y4R, shown in Fig. 8c, the result of the proposed method, shown in Fig. 8b, shows high performance on distinguishing the forest area (green) and the city area (red and pink). The Tokyo harbor area shown in Fig. 9a includes a large city area with many isolated man-made targets (bridges). The result of the proposed method, shown in Fig. 9b can interpret this area significantly informatively compared with the result of Y4R shown in Fig. 9c. In Fig. 9c, large areas of randomly distributed buildings and isolated man-made targets show volume scattering which is near to that of some natural targets such as forests. The proposed method, in contrast, the city areas are identified clearly. The origin of the strength of the proposed method for detecting man-made targets lies in the fact that it focuses on target structures rather than only scattering mechanisms themselves.

VI. CONCLUSION

We have proposed a new PolSAR data interpretation method based on averaged Stokes vector. First, we have extracted five discriminators from the averaged Stokes vector to describe the structure and scattering mechanism information of the

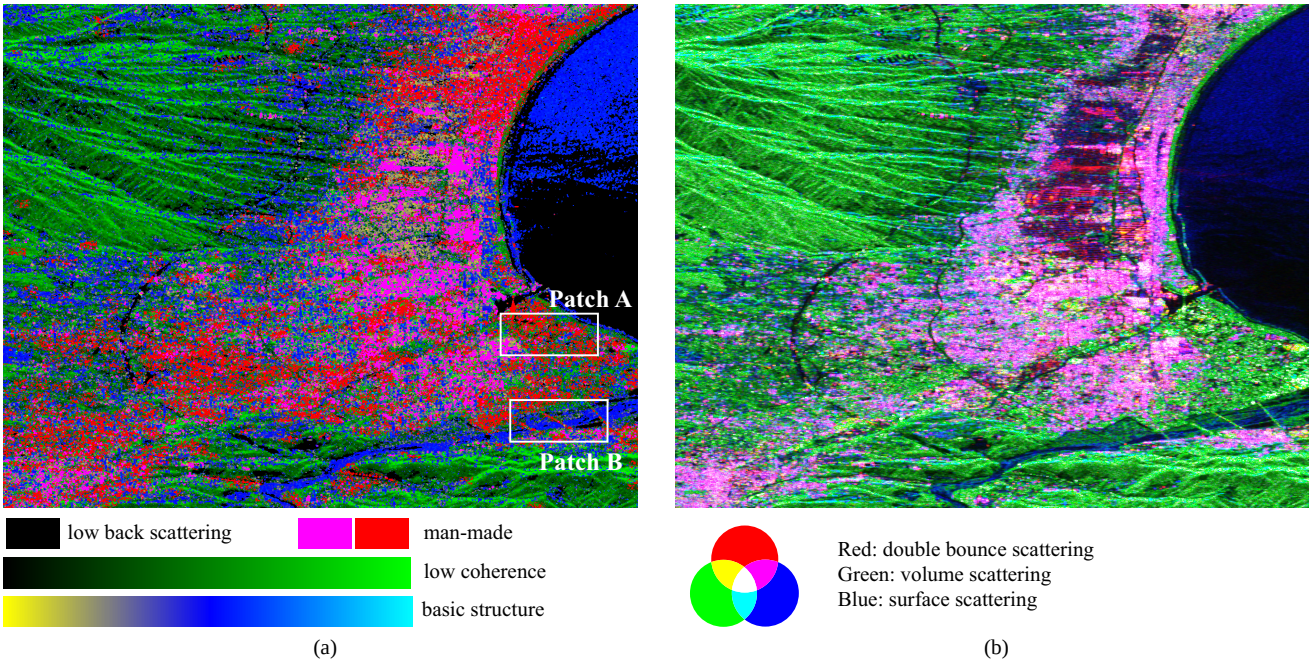

Fig. 6. Interpretation results generated by ALOS-PALSAR data of (a) the proposed method with thresholds: $\delta_\rho = 0.5$, $\delta_h = 0.3$, $\delta_w = 0.4$, $\delta_A = 0.2$, and patch size of W: 15×60, and (b) the Y4R method, for Suruga bay area.

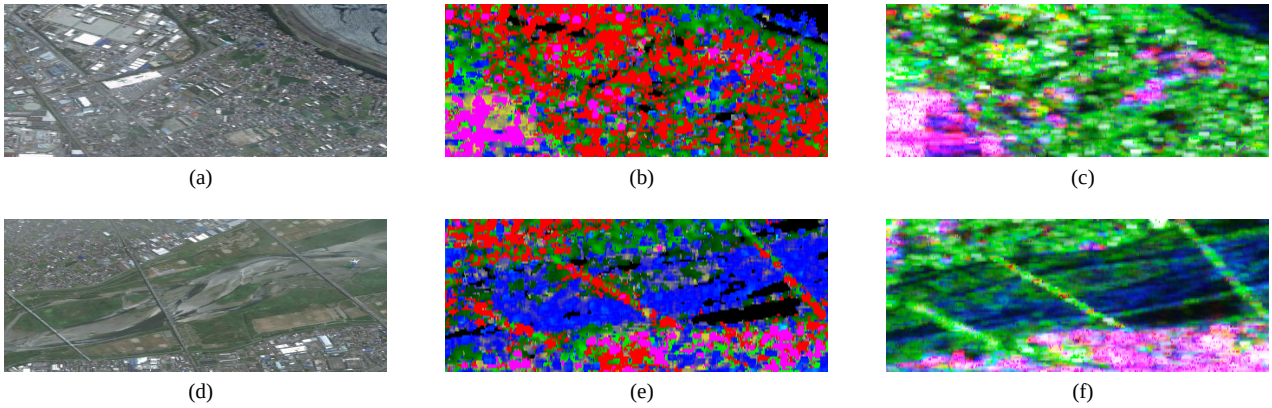

Fig. 7. (a) Google satellite photo for patch A; (b) interpretation result of the proposed method for patch A; (c) interpretation result of the Y4R method; (d) Google satellite photo for patch B; (e) interpretation result of the proposed method for patch B; (f) interpretation result of the Y4R method for patch B.

targets. Based on the extracted discriminators, we have built four physical interpretation layers with ascending priorities: the basic layer, the low coherence targets layer, the man-made targets layer, and the low back scattering targets layer. An intuitive final image have been generated by simply stacking the four layers in the priority order. The experiments have been done over ALOS-PALSAR data. The results for Suruga bay area, Ebetsu city area and Tokyo harbor area have shown that the proposed method has high interpretation performance, especially for skew aligned or randomly distributed man-made targets as well as isolated man-made targets. The origin of the strength of the proposed method for detecting man-made targets lies in the fact that it focuses on target structures rather than only scattering mechanisms themselves.

Appendix A
Proof of the Statement that Ideal Routes are Circular Arcs

An ideal route can be perfectly related to a scattering matrix. Note the scattering matrix as

$$S_0 = \begin{bmatrix} a & b \\ c & d \end{bmatrix}, \tag{23}$$

where a, b, c, and d are complex numbers. Take the ideal zero aperture route as an example. The zero aperture route is composed by all the polarization state points for linearly polarized incident waves $[\cos\phi, \sin\phi]^T$. For a certain polarization angle ϕ, the coordinate of the corresponding point in the zero aperture route is $(g_1/g_0, g_2/g_0, g_3/g_0)$, where g_0, g_1, g_2, and

(a)

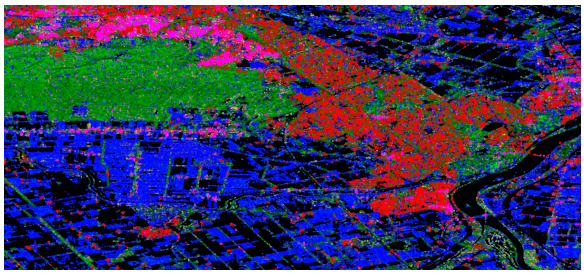

(b)

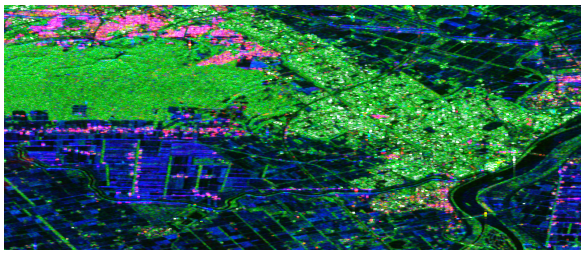

(c)

Fig. 8. (a) Google satellite photo, and interpretation results generated by ALOS-PALSAR data of (b) the proposed method with thresholds: $\delta_\rho = 0.5$, $\delta_h = 0.3$, $\delta_w = 0.4$, $\delta_A = 0.2$, and patch size of W: 15×60, and (c) the Y4R method, for Ebetsu city area.

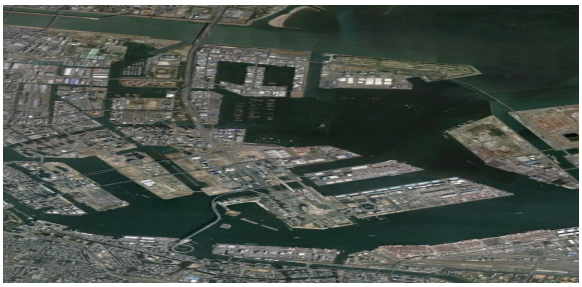

(a)

(b)

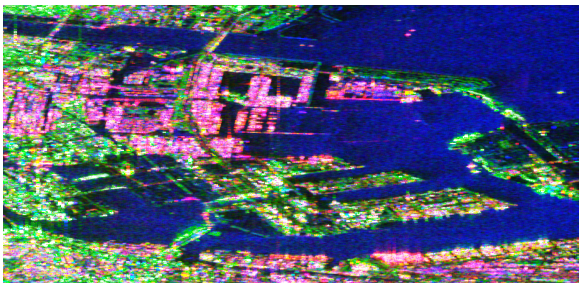

(c)

Fig. 9. (a) Google satellite photo, and interpretation results generated by ALOS-PALSAR data of (b) the proposed method with thresholds: $\delta_\rho = 0.5$, $\delta_h = 0.3$, $\delta_w = 0.4$, $\delta_A = 0.2$, and patch size of W: 15×60, and (c) the Y4R method, for Tokyo harbor area.

g_3 are calculated as

$$\begin{aligned}
g_0 &= \left(|a|^2 + |c|^2\right)\cos^2\phi + \left(|b|^2 + |d|^2\right)\sin^2\phi \\
&\quad + \left(ab^* + a^*b + cd^* + c^*d\right)\sin\phi\cos\phi \\
g_1 &= \left(|a|^2 - |c|^2\right)\cos^2\phi + \left(|b|^2 - |d|^2\right)\sin^2\phi \\
&\quad + \left(ab^* + a^*b - cd^* - c^*d\right)\sin\phi\cos\phi \\
g_2 &= \left(ac^* + a^*c\right)\cos^2\phi + \left(bd^* + b^*d\right)\sin^2\phi \\
&\quad + \left(ad^* + a^*d + bc^* + b^*c\right)\sin\phi\cos\phi \\
g_3 &= j\left(ac^* - a^*c\right)\cos^2\phi + j\left(bd^* - b^*d\right)\sin^2\phi \\
&\quad + j\left(ad^* - a^*d + bc^* - b^*c\right)\sin\phi\cos\phi
\end{aligned} \tag{24}$$

We can simplify the expression as

$$\begin{aligned}
g_0 &= A_0 t + B_0 p + C_0 q, \\
g_1 &= A_1 t + B_1 p + C_1 q, \\
g_2 &= A_2 t + B_2 p + C_2 q, \\
g_3 &= A_3 t + B_3 p + C_3 q,
\end{aligned} \tag{25}$$

where $A_i, B_i, C_i, i = 0, 1, 2, 3$ are constants determined by the scattering matrix, and $t = \cos^2\phi$, $p = \sin^2\phi$, and $q = \sin\phi\cos\phi$ are variables of ϕ.

Thus, for three different points, $G^{(1)}$, $G^{(2)}$, and $G^{(3)}$, in the zero aperture route, the normal vector $\hat{n}$ of the plane determined by these three points is calculated as

$$\begin{aligned}
\hat{n} &= \left(G^{(1)} - G^{(2)}\right) \times \left(G^{(1)} - G^{(3)}\right) \\
&= G^{(1)} \times G^{(2)} + G^{(2)} \times G^{(3)} + G^{(3)} \times G^{(1)} \\
&= \frac{1}{g_0^{(1)} g_0^{(2)} g_0^{(3)}} \left(\hat{n}_1, \hat{n}_2, \hat{n}_3\right),
\end{aligned} \tag{26}$$

where $\times$ indicates the outer product of two vectors, and

$$\begin{aligned}
\hat{n}_1 &= \sum_{(i,j,k)} \left(g_2^{(i)} g_3^{(j)} - g_3^{(i)} g_2^{(j)}\right) g_0^{(k)}, \\
\hat{n}_2 &= \sum_{(i,j,k)} \left(g_3^{(i)} g_1^{(j)} - g_1^{(i)} g_3^{(j)}\right) g_0^{(k)}, \\
\hat{n}_3 &= \sum_{(i,j,k)} \left(g_1^{(i)} g_2^{(j)} - g_2^{(i)} g_1^{(j)}\right) g_0^{(k)}.
\end{aligned} \tag{27}$$

Equation (27) shows that $\hat{n}_1$, $\hat{n}_2$, and $\hat{n}_3$ have similar expressions. Note that, (i, j, k) is an ordered group which can be $(1, 2, 3)$, $(2, 3, 1)$, or $(3, 1, 2)$. First, we focus on $\hat{n}_1$. According to (25) and (27), the final expansion of $\hat{n}_1$ is

$$\begin{aligned}\hat{n}_1 = \sum_{(i,j,k)} \big[&(A_2B_3C_0 - A_3B_2C_0)\left(t^{(i)}p^{(j)}q^{(k)} - p^{(i)}t^{(j)}q^{(k)}\right) \\ &+ (A_2B_0C_3 - A_3B_0C_2)\left(t^{(i)}q^{(j)}p^{(k)} - q^{(i)}t^{(j)}p^{(k)}\right) \\ &+ (A_0B_2C_3 - A_0B_3C_2)\left(p^{(i)}q^{(j)}t^{(k)} - q^{(i)}p^{(j)}t^{(k)}\right)\big] \\ =&K_1 f_\phi,\end{aligned} \tag{28}$$

where $K_1 = (A_2B_3C_0 - A_3B_2C_0) - (A_2B_0C_3 - A_3B_0C_2) + (A_0B_2C_3 - A_0B_3C_2)$ is only determined by the scattering matrix. $f_\phi = \sum_{(i,j,k)} \left(t^{(i)}p^{(j)}q^{(k)} - p^{(i)}t^{(j)}q^{(k)}\right)$ is only determined by $\phi^{(1)}$, $\phi^{(2)}$, and $\phi^{(3)}$. Similarly, we can prove that $\hat{n}_2 = K_2 f_\phi$, and $\hat{n}_3 = K_3 f_\phi$. Thus, according to (26), the norm vector $\hat{n}$ can be expressed as

$$\begin{aligned}\hat{n} &= \frac{1}{g_0^{(1)} g_0^{(2)} g_0^{(3)}} \left(K_1 f_\phi, K_2 f_\phi, K_3 f_\phi\right) \\ &= \frac{f_\phi}{g_0^{(1)} g_0^{(2)} g_0^{(3)}} \left(K_1, K_2, K_3\right).\end{aligned} \tag{29}$$

Equation (28) shows that, the direction of $\hat{n}$ is determined by K_1, K_2, and K_3. It means that, the direction of $\hat{n}$ is independent of ϕ. Therefore, for any different three points in the ideal zero aperture route, the norm vector of the surface determined by them has identical direction determined by the scattering matrix. It is proved that, all the points in the ideal zero aperture route are in the same plane. Similarly, we can also prove that all the points in ideal zero orientation route are in the same plane. Since the routes are on the surface of Poincare sphere, the ideal routes should be circular arcs.

REFERENCES

[1] S. R. Cloude and E. Pottier, "A review of target decomposition theorems in radar polarimetry," *IEEE Trans. Geosci. Remote Sens.*, vol. 34, pp. 498–518, 1996.

[2] J. S. Lee, W. M. Boerner, D. L. Schuler, T. L. Ainsworth, I. Hajnsek, K. P. Papathanassiou, and E. Luneburg, "A review of polarimetric SAR algorithms and their applications," *Journal of Photogrammetry and Remote Sensing*, vol. 9, pp. 31–80, 2004.

[3] R. Touzi, W. M. Boerner, J. S. Lee, and E. Lueneburg, "A review of polarimetry in the context of synthetic aperture radar: Concepts and information extraction," *Can. J. Remote Sensing*, vol. 30, pp. 380–407, 2004.

[4] A. Freeman, "Fitting a two-component scattering model to polarimetric SAR data from forests," *IEEE Trans. Geosci. Remote Sens.*, vol. 45, pp. 2583–2592, 2007.

[5] A. Freeman and S. L. Durden, "A three-component scattering model for polarimetric SAR data," *IEEE Trans. Geosci. Remote Sens.*, vol. 36, pp. 963–973, 1998.

[6] S. R. Cloude and E. Pottier, "An entropy based classification scheme for land applications of polarimetric SAR," *IEEE Trans. Geosci. Remote Sens.*, vol. 35, pp. 68–78, 1997.

[7] Y. Yamaguchi, T. Moriyama, M. Ishido, and H. Ymada, "Four-component scattering model for polarimetric SAR image decomposition," *IEEE Trans. Geosci. Remote Sens.*, vol. 43, pp. 1699–1706, 2005.

[8] J. Yang, Y. N. Peng, Y. Yamaguchi, and H. Yamada, "On huynen's decomposition of a kennaugh matrix," *IEEE Geosci. Remote Sens. Lett.*, vol. 3, pp. 369–372, 2006.

[9] Y. Yamaguchi, Y. Yajima, and H. Ymada, "A four-component decomposition of PolSAR images based on the coherency matrix," *IEEE Geosci. Remote Sens. Lett.*, vol. 3, pp. 292–296, 2006.

[10] Y. Yamaguchi, A. Sato, W. M. Boerner, R. Sato, and H. Yamada, "Four-component scattering power decomposition with rotation of coherency matrix," *IEEE Trans. Geosci. Remote Sens.*, vol. 49, pp. 2251–2258, 2011.

[11] Y. Cui, Y. Yamaguchi, J. Yang, H. Kobayashi, and S. E. Park, "On complete model-based decomposition of polarimetric SAR coherency matrix data," *IEEE Transactions on Geoscience and Remote Sensing*, vol. 52, pp. 1991–2001, 2014.

[12] R. K. Raney, "Dual-polarized SAR and stokes parameters," *IEEE Geosci. Remote Sens. Lett.*, vol. 3, pp. 317–319, 2006.

[13] R. Touzi, S. Goze, T. L. Toan, A. Lopes, and E. Mougin, "Polarimetric discriminators for SAR images," *IEEE Trans. Geosci. Remote Sens.*, vol. 30, pp. 973–980, 1992.

[14] J. J. van Zyl, M. Arii, and Y. J. Kim, "Model-based decomposition of polarimetric SAR covariance matrices constrained for nonnegative eigenvalues," *IEEE Trans. Geosci. Remote Sens.*, vol. 49, pp. 3452–3459, 2011.

[15] M. Arii, J. J. van Zyl, and Y. J. Kim, "Adaptive model-based decomposition of polarimetric SAR covariance matrices," *IEEE Trans. Geosci. Remote Sens.*, vol. 49, pp. 1104–1113, 2011.

[16] Z. L. Shan, C. Wang, H. Zhang, and W. T. An, "Improved four-component model-based target decomposition for polarimetric SAR data," *IEEE Geosci. Remote Sens. Lett.*, vol. 9, pp. 75–79, 2012.

[17] Z. H. Jiao, J. Yang, C. M. Yeh, and J. S. Song, "Modified three-component decomposition method for polarimetric SAR data," *IEEE Geosci. Remote Sens. Lett.*, vol. 11, pp. 200–204, 2014.

[18] G. Singh, Y. Yamaguchi, and S. E. Park, "General four-component scattering power decomposition with unitary transformation of coherency matrix," *IEEE Trans. Geosci. Remote Sens.*, vol. 51, pp. 3014–3022, 2013.

[19] F. Shang and A. Hirose, "Considerations on C/T matrix-based PoLSAR land classification and explorations on stokes vector based method," in *IEEE International Geoscience and Remote Sensing Symposium*, 2014, pp. 4576–4579.

[20] D. L. Evans, T. G. Farr, J. J. V. Zyl, and H. A. Zebker, "Radar polarimetry: Analysis tools and applications," *IEEE Trans. Geosci. Remote Sens.*, vol. 26, pp. 774–789, 1988.

[21] M. Born and E. Wolf, *Principles of Optics: Electromagnetic Theory of Propagation, Interference and Diffraction of Light (7th edition)*. Cambridge University Press, 1999.

[22] R. Shirvany, M. Chabert, and J. Y. Tourneret, "Ship and oil-spill detection using the degree of polarization in linear and hybrid/compact dual-PolSAR," *IEEE Journal of Selected Topics in Applied Earth Observations and Remote Sensing*, vol. 5, pp. 885–892, 2012.

[23] F. Shang and A. Hirose, "Quaternion neural-network-based polsar land classification in poincare-sphere-parameter space," *IEEE Transactions on Geoscience and Remote Sensing*, vol. 52, pp. 5693 – 5703, 2014.

[24] ——, "Use of poincare sphere parameters for fast supervised PolSAR land classification," in *IEEE International Geoscience and Remote Sensing Symposium*, 2013, pp. 3175–3178.

[25] ——, "PolSAR land classification by using quaternion-valued neural networks," in *Asia-Pacific Conference on Synthetic Aperture Radar*, 2013, pp. 593–596.

[26] M. Shimoni, D. Borghys, R. Heremans, C. Perneel, and MoAcheroy, "Fusion of PolSAR and PolInSAR data for land cover classification," *International Journal of Applied Earth Observation and Geoinformation*, vol. 11, pp. 169–180, 2009.

[27] F. D. Frate, A. Petrocchi, J. Lichtenegger, and G. Calabresi, "Neural networks for oil spill detection using ERS-SAR data," *IEEE Trans. Geosci. Remote Sens.*, vol. 37, pp. 2249–2258, 1999.

[28] J. S. Lee, M. R. Grunes, T. L. Ainsworth, L. J. Du, and S. R. Cloude, "Unsupervised classification using polarimetric decomposition and the complex wishart classifier," *IEEE Trans. Geosci. Remote Sens.*, vol. 37, pp. 2249–2258, 1999.

[29] S. E. Park and W. M. Moon, "Unsupervised classification of scattering mechanisms in polarimetric SAR data using fuzzy logic in entropy and alpha plane," *IEEE Trans. Geosci. Remote Sens.*, vol. 45, pp. 2652–2664, 2007.

Fang Shang (M'15) received the B.S. and M.S. degree in electrical engineering and automation from Harbin Institute of Technology, China, in 2009 and 2011. She received the Ph.D degree in electrical engineering and information systems from The University of Tokyo, Japan, in 2014.

Dr. Shang is an Assistant Professor in the Graduate School of Informatics and Engineering, University of Electro-Communications, Japan. Her current research interest is in the signal and imaging processing for the polarimetric SAR and the UWB radar.

Akira Hirose (F'13) received the Ph.D. degree in electronic engineering from The University of Tokyo, Tokyo, Japan, in 1991. In 1987, he joined the Research Center for Advanced Science and Technology (RCAST), The University of Tokyo, as a Research Associate. In 1991, he was appointed as an Instructor at the RCAST. From 1993 to 1995, on leave of absence from The University of Tokyo, he joined the Institute for Neuroinformatics, University of Bonn, Bonn, Germany. From 2006 to 2008, he was also an Affiliate Professor of Institute of Space and Astronautical Science (ISAS), Japan Aerospace Exploration Agency (JAXA). He is currently a Professor with the Department of Electrical Engineering and Information Systems, The University of Tokyo. The main fields of his research interest are wireless electronics and neural networks.

Dr. Hirose is a Senior Member of the Institute of Electronics, Information and Communication Engineers (IEICE) and a member of the Japanese Neural Network Society (JNNS). He served as the Editor-in-Chief of the IEICE Transactions on Electronics, an Associate Editor of journals such as the IEEE TRANSACTIONS ON NEURAL NETWORKS and the IEEE GEOSCIENCE AND REMOTE SENSING NEWSLETTER, the Chair of the Neurocomputing Technical Group in the IEICE and the General Chair of the 2013 Asia-Pacific Conference on Synthetic Aperture Radar (APSAR) in Tsukuba. He currently serves as a member of the IEEE Computational Intelligence Society (CIS) Neural Networks Technical Committee, the Governing Board Member of the Asia-Pacific Neural Network Assembly, the Vice President of the IEICE Electronics Society, the President of the JNNS, the Chair of IEEE GRSS All Japan Chapter, and an IEEE GRSS Distinguished Lecturer.